

# Gaussian Thermionic Emission Model for Analysis of Au/MoS<sub>2</sub> Schottky-Barrier Devices

Calvin Pei Yu Wong<sup>1,2,3,\*</sup>, Cedric Troadec<sup>1,2</sup>, Andrew T.S. Wee<sup>1,2</sup>, and Kuan Eng Johnson Goh<sup>1,2,3,†</sup>

<sup>1</sup>*NUS Graduate School for Integrative Sciences and Engineering, National University of Singapore, Centre for Life Sciences, #05-01, 28 Medical Drive, Singapore 117456, Singapore*

<sup>2</sup>*Institute of Materials Research and Engineering, A\*STAR (Agency for Science, Technology and Research), 2 Fusionopolis Way, #08-03 Innovis, Singapore 138634, Singapore*

<sup>3</sup>*Department of Physics, Faculty of Science, National University of Singapore, 2 Science Drive 3, Singapore 117551, Singapore*

(Received 9 August 2020; revised 17 September 2020; accepted 21 September 2020; published 12 November 2020)

Schottky-barrier inhomogeneities are expected at the metal–transition-metal-dichalcogenide (TMDC) interface and this can impact device performance. However, it is difficult to account for the distribution of interface inhomogeneity as most techniques average over the spot area of the analytical tool (e.g., few hundred micrometers squared for photoelectron-based techniques), or the entire device measured for electrical current-voltage (*I*-*V*) measurements. Commonly used models to extract Schottky-barrier heights neglect or fail to account for such inhomogeneities, which can lead to the extraction of incorrect Schottky-barrier heights and Richardson constants that are orders of magnitude away from theoretically expected values. Here, we show that a Gaussian-modified thermionic emission model gives the best fit to experimental temperature-dependent current-voltage (*I*-*V*-*T*) data of van der Waals Au/*p*-MoS<sub>2</sub> interfaces and allow the deconvolution of the Schottky-barrier heights of the defective regions from the pristine region. By the inclusion of a Gaussian-distributed Schottky-barrier height in the macroscopic *I*-*V*-*T* analysis, we demonstrate that interface inhomogeneities due to defects are deconvoluted and well correlated to the impact on the device behavior across a wide temperature range from a room temperature of 300 K down to 120 K. We verify the Gaussian thermionic model across two different types of *p*-MoS<sub>2</sub> (geological bulk crystals and synthetic flux-grown crystals), and finally compare the macroscopic Schottky-barrier heights with the results of a nanoscopic technique, ballistic hole emission microscopy (BHEM). The results obtained using BHEM are consistent with the pristine Au/*p*-MoS<sub>2</sub> Schottky-barrier height extracted from the Gaussian-modified thermionic emission model over hundreds of nanometers. Our findings show that the inclusion of Schottky-barrier inhomogeneities in the analysis of *I*-*V*-*T* data is useful to elucidate the impact of defects (e.g., grain boundaries, metallic impurities, etc.) and hence their influence on device behavior. We also find that the effective Richardson constant, a material-specific constant typically treated as merely a fitting constant, is a useful parameter to check for the validity of the transport model.

DOI: 10.1103/PhysRevApplied.14.054027

## I. INTRODUCTION

Schottky-barrier inhomogeneities are present at the metal–transition-metal-dichalcogenide (TMDC) interface due to potential fluctuations and defects in the material and this can impact the device performance [1–4]. However, the most commonly used thermionic emission transport

model modified with a simple ideality factor correction [5] does not account sufficiently for nonideal effects such as inhomogeneities, often leading to the extraction of an apparent Schottky-barrier height (SBH) convoluted with other factors such as defects (inhomogeneity) and temperature. The extracted apparent SBH from the simple model does not represent the true band alignment at the metal-semiconductor interface and is counterproductive to the correct understanding of the energetics of the interface. Several other models have been proposed to account for these nonideal effects in the current-voltage (*I*-*V*) behavior of Schottky-barrier devices [1–8]. In this paper, we compare the effectiveness of four types of commonly used transport models to extract correct values of the SBH and the material-specific Richardson constant of MoS<sub>2</sub>. We

\*calvin\_wong@imre.a-star.edu.sg

†kejgoh@yahoo.com

Published by the American Physical Society under the terms of the [Creative Commons Attribution 4.0 International](#) license. Further distribution of this work must maintain attribution to the author(s) and the published article's title, journal citation, and DOI.

verify the SBH extracted from the transport models against the SBH obtained from ballistic hole emission microscopy (BHEM) [9–11], which is a direct measurement method for the SBH at the nanoscale, and verify the Richardson constants extracted from the models with theoretical calculated values based on the electron (hole) effective mass of MoS<sub>2</sub> [12,13]. Finally, we compare the SBH and Richardson constants across two types of MoS<sub>2</sub> (geological bulk crystals and synthetic flux grown bulk crystals) from different sources and show that the SBH and Richardson constants are similar across the two MoS<sub>2</sub> devices if analyzed using the correct model.

The transport of thermally activated carriers across a typical metal-semiconductor Schottky interface where the semiconductor is lightly doped (approximately 10<sup>15</sup> to 10<sup>17</sup> cm<sup>-3</sup>) is given by the ideal thermionic emission model [Eq. (1)] [5].

$$I = I_S \left[ \exp \left( \frac{qV}{kT} \right) - 1 \right], \quad (1)$$

where

$$I_S = \left[ A A^{**} T^2 \exp \left( -\frac{q\phi}{kT} \right) \right] \quad (2)$$

and  $q$  is the electric charge,  $V$  the voltage applied across the diode,  $k$  the Boltzmann constant,  $T$  the absolute temperature,  $A$  the area of the diode,  $A^{**}$  the effective Richardson constant of the semiconductor, and  $\phi$  the Schottky-barrier height. A requirement of this model is that the tunneling of carriers across the Schottky barrier is negligible, which is valid when the semiconductor is lightly doped (approximately 10<sup>15</sup> to 10<sup>17</sup> cm<sup>-3</sup>) such that the band banding is gradual and the Schottky-barrier width is wide. The accurate extraction of the SBH depends greatly on the successful determination of  $I_S$  from the forward-bias slope of the experimental  $I$ - $V$  curves [Eq. (1)]. However, the thermionic emission model does not fit well to experimental  $I$ - $V$  curves at low temperatures, and the modified (nonideal) thermionic emission models [6,7], the thermionic field emission (thermally assisted tunneling) model or the generation-recombination model are often used instead [14,15]. While these modified models seem to fit certain experimental datasets well, the numbers that have been extracted have not always been reliable. For instance, negative SBHs have been reported [16,17], but negative SBHs have no physical meaning and show that the models are not suitable for these specific devices, and other material-specific constants such as the Richardson constants are orders of magnitude away from the theoretically derived values [6,7]. Hence, it is not trivial to identify a correct model to accurately extract the SBH of metal-semiconductor Schottky interfaces, especially if the

measurement is done at a specific, or a small range of temperatures, as the effect of temperature can be convoluted into the extracted SBH.

In this paper, we investigate the use of four well-established methods for extracting Schottky-barrier heights as a function of temperature from a weakly interacting van der Waals Au contact to a layered MoS<sub>2</sub> crystal. The epitaxial growth of Au on MoS<sub>2</sub> allows a clean and abrupt interface for this material system [18], similar to recent reports of fabricating a van der Waals metal-TMD interface [19,20], making it an ideal model system for this study. Four methods are used to extract SBH from temperature-dependent  $I$ - $V$  ( $I$ - $V$ - $T$ ) curves: method 1: the standard Richardson plot  $\ln(I_S/T^2)$  vs  $1/T$  [5]; method 2: the modified Richardson (Hackam and Haarop) plot  $\ln(I_S/T^2)$  vs  $1/nT$  [8]; method 3: the modified Richardson (Bhuiyan) plot  $n \ln(I_S/T^2)$  vs  $1/T$  [6]. From this comparison, we show that none of these three methods provide a satisfactory fit, while a fourth method, method 4, the Gaussian thermionic emission model [4], provides the best fit across a wide temperature regime of 120 to 300 K across two different types (geological bulk crystals and synthetic flux grown bulk crystals) of MoS<sub>2</sub> samples. To date, although the Gaussian thermionic model has shown much success in fitting experimental data to metal/MoS<sub>2</sub> Schottky devices [21,22], this model has not been compared directly across samples of different origins and explicitly verified with a complementary technique, such as ballistic electron (hole) emission microscopy [9,10,23], which is a direct measurement of the nanoscale unbiased SBH. The aim of this paper is to review and compare these analysis methods in the context of a clean van der Waals epitaxial contact to a layered material, and show that using the inadequate model in the analysis of temperature dependent  $I$ - $V$  data can yield Schottky-barrier height values that are misleading by up to an order of magnitude and counterproductive to the understanding of the Schottky interface. We show that the effective Richardson constant ( $A^{**}$ ), typically treated as a fitting constant is a useful parameter to cross-check the validity of the transport model. As field-effect transistors based on two-dimensional (2D) TMDs such as MoS<sub>2</sub> and WS<sub>2</sub> have been shown to behave as Schottky-barrier transistors [24–26], where the Schottky barrier at the metal-semiconductor contact is modulated by the gate bias, the correct analysis of the Schottky barrier is crucial to the understanding of the subthreshold behavior of these 2D transistors, especially in the presence of defects [27–29].

## A. Methods to extract the Schottky-barrier height

The thermionic emission model, Eq. (1), predicts that for  $V > 3kT/q$ , a plot of  $\ln I$  against  $V$  will be linear with a slope of 1 and its intercept at  $V=0$  will give  $I_S$ . From  $I_S$ , the Schottky-barrier height can be extracted.

A direct reading of  $I_S$  from the experimental  $I$ - $V$  curve is typically not used as the experimental reverse-biased saturation current, as it also contains the image-force lowering and other minority carrier effects [5]. However, the thermionic emission model is inadequate for a realistic metal-semiconductor interface especially at low temperatures. To account for the nonideal transport mechanisms, and series resistance in real devices, the ideality factor  $n$  and the series resistance  $R_s$ , are empirically added to the model [5,30] and Eq. (1) becomes

$$I = I_S \left[ \exp \left( \frac{q(V - IR_s)}{nkT} \right) - 1 \right]. \quad (3)$$

Using the modified thermionic emission model, diode parameters such as the ideality factor  $n$  and barrier height  $\phi$  can be plotted and are found to be dependent on the temperature. At low temperatures, the thermionic emission model does not fit well to the experimental data and  **$n$  increases greatly beyond 1, signifying nonideal transport**. While the **nonideal** transport has been attributed to additional current contributions from **thermally assisted tunneling (thermionic field emission) across the Schottky barrier, generation-recombination current in the depletion region and image-force lowering**, it is not clear how the empirically modified thermionic emission model can account for these effects. From these modifications, a few versions of the Richardson plot are analyzed.

### B. Method 1: ideal Richardson plot ( $\ln I_S/T^2$ vs $1/T$ )

This is the simplest method and is derived directly from the saturation current term of the thermionic emission model, Eq. (2). When temperature-dependent plots can be obtained, a plot of  $\ln(I_S/T^2)$  vs  $1/T$ , called a Richardson plot, will be a straight line where the slope and intercept at  $1/T=0$  will give  $\phi$ , and  $A^{**}$ , respectively. The empirically added ideality factor is not included in Eq. (2), hence this method is the ideal Richardson plot analysis.

### C. Method 2: ideality-factor-modified Richardson plot I ( $\ln I_S/T^2$ vs $1/nT$ )

To account for effects that cause deviations from ideal ( $n=1$ ) behavior, such as the image force and surface charges, which they argued to be also present at zero bias, Hackam and Harrop proposed a modified Richardson plot from Eq. (3) to include the ideality factor in the  $I_S$  term [8]. The forward current appears as

$$I = \left[ AA^{**}T^2 \exp \left( -\frac{q\phi}{nkT} \right) \right] \left[ \frac{q(V - IR_s)}{nkT} - 1 \right]. \quad (4)$$

The addition of  $n$  to the  $I_S$  term in Eq. (4) now gives a modified Richardson plot Eq. (5) from which the SBH can

be extracted from the gradient of the straight line and  $A^{**}$  from the  $y$  intercept.

$$\ln \frac{I_S}{T^2} = \ln AA^{**} - \frac{q\phi}{nkT}. \quad (5)$$

### D. Method 3: ideality-factor-modified Richardson plot II ( $n \ln I_S/T^2$ vs $1/T$ )

Bhuiyan, Martinez, and Esteve found that the Hackam and Harrop model does not work for them due to the presence of a strongly temperature-dependent SBH and ideality factor measured [6] and that the  $A^{**}$  extracted from using the Hackam and Harrop method is too large. Hence, they empirically proposed Eq. (6):

$$I = \left[ AA^{**}T^2 \exp \left( -\frac{q\phi}{nkT} \right) \right] \left[ \exp \left( \frac{q(V - IR_s)}{kT} \right) - 1 \right]. \quad (6)$$

Following their modification, the modified Richardson plot now reads

$$n \ln \frac{I_S}{T^2} = \ln AA^{**} - \frac{q\phi}{kT}. \quad (7)$$

### E. Method 4: inhomogeneous Gaussian-barrier-modified Richardson plot

Two different inhomogeneous Schottky-barrier models have been proposed independently by Werner and Gütter [3,4], and Tung and coworkers [2,31]. Werner and Gütter used a Gaussian approximation of the SBH distribution to account for the potential fluctuations at the interface, while Tung used a generalized model. While Tung's model is more rigorous, Werner and Gütter's model is simpler and can be placed into the context of BHEM-measured SBHs. Hence in this paper, we focus on the Werner and Gütter model of Gaussian SBH [4], which is given by

$$\phi^{app} = \Phi - \frac{\sigma^2}{2kT/q}, \quad (8)$$

where  $\phi^{app}$  is the apparent Schottky-barrier height obtained as a result of the convolution of the Gaussian-distributed SBH with temperature in the thermionic emission model,  $\Phi$  is the mean Schottky-barrier height and  $\sigma$  is the standard deviation of the Gaussian distribution. To obtain the  $\sigma$  of the Gaussian, a plot of  $\phi^{app}$  against  $1/T$  can be used. The Gaussian standard deviations ( $\sigma$ ) extracted from Eq. (8) can then be used to correct for the Gaussian-distributed SBH to obtain the Gaussian-corrected Richardson plots Eq. (9). Here, a plot of  $\ln(I_S/T^2) - [(q^2\sigma^2)/(2k^2T^2)]$  against  $1/T$  will give the  $A^{**}$  in the intercept and  $\Phi$  in

the gradient.

$$\ln\left(\frac{I_S}{T^2}\right) = \ln AA^{**} - \frac{q\Phi}{kT} + \frac{q^2\sigma^2}{2k^2T^2}. \quad (9)$$

The temperature dependence of the ideality factor and SBH, initially viewed as empirical inconsistencies in many experiments, is now well explained by Werner and Gütter to arise from the inhomogeneous SBH and that capacitance-voltage (*C-V*) measurements give  $\Phi$ . In our experiments, we do not perform *C-V* measurements as capacitance measurement is not typically used in the operation of devices, but the current as a function of applied voltage (*I-V*) is used and is more common for analysis. Werner and Gütter also showed that for lightly doped ( $10^{15}$  to  $10^{17}$  cm $^{-3}$ ) semiconductors, thermionic emission dominates carrier transport, even at low temperatures down to 77 K.

We demonstrate in our Au/MoS<sub>2</sub> sample that by using a Gaussian-distributed SBH to account for these inhomogeneities, a more reliable value of the SBH can be obtained. We verify the Gaussian thermionic emission model systematically using two different types of MoS<sub>2</sub> (geological bulk crystals and synthetic flux-grown bulk MoS<sub>2</sub> crystals, from Ward's Science [32] and 2D semiconductors [33], respectively) by performing temperature-dependent current-voltage measurements (*I-V-T*). We show that the  $A^{**}$ , a useful material-specific constant dependent only on the electron effective mass, though commonly treated as merely a fitting constant, can be a useful parameter to cross-check the validity of the model. Therefore, obtaining Richardson plots for these devices is key. To further validate the use of the Gaussian thermionic emission model, we compare the extracted mean SBH ( $\Phi$ ) with a complementary technique, ballistic hole emission microscopy (BHEM) and show that the SBH values obtained are identical within error limits across the two different samples and complementary techniques. We propose that the Gaussian thermionic emission model gives a more accurate representation of the real Schottky interface and our results can be used to reconcile the conflicting reports on SBH in the literature and allow *I-V-T* analysis to yield more in-depth understanding of the interface.

## II. EXPERIMENTAL DESIGN

Figure 1 shows a schematic of the fabricated Au/MoS<sub>2</sub> Schottky diode and the corresponding scanning electron microscope (SEM) image. We use the bulk MoS<sub>2</sub> crystal as the device material to allow clean shadow-mask fabrication and the metal-semiconductor interface formed with the top layer can provide the basic understanding of metal contacts to layered semiconductor devices. Ti is chosen as the Ohmic contact as it is a commonly used material for Ohmic contacts to MoS<sub>2</sub>. We choose Au as the Schottky contact as it is a high-work-function metal that is not

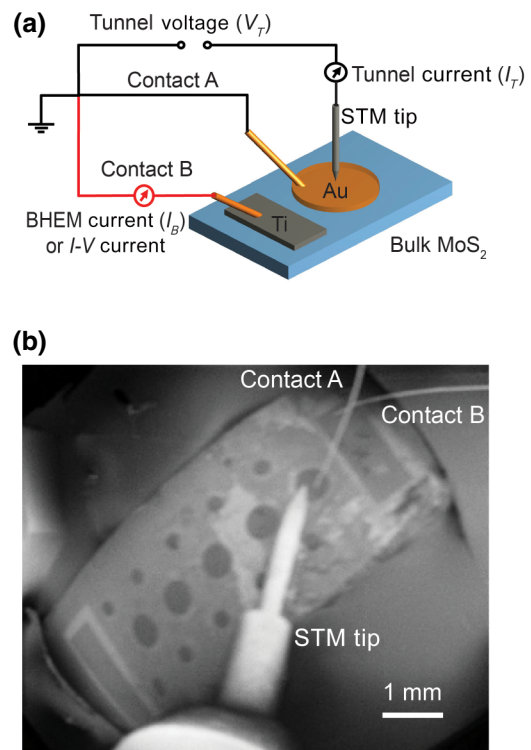


FIG. 1. (a) Schematic of the Au/MoS<sub>2</sub> device. Contacts A and B are used to perform *I-V* measurements and the scanning tunneling microscope (STM) tip is added for BHEM measurements, (b) the corresponding scanning electron microscope showing actual device during BHEM measurements. Imaging conditions: 0.1-kV acceleration voltage, 20-pA current.

expected to form Ohmic contacts with MoS<sub>2</sub> without interface modification, and it is also a commonly used contact material in the literature due to its inertness in the ambient environment.

## III. EXPERIMENT

The *p*-type geological bulk MoS<sub>2</sub> crystal is obtained from Ward's Science [32], the *p*-type synthetic flux-grown MoS<sub>2</sub> crystal (intrinsic) is obtained from 2D semiconductors [33]. The Ohmic contacts to the MoS<sub>2</sub> crystals are deposited in a high vacuum *e*-beam evaporator system (AJA International) after cleaving off the top surface using sticky tape to obtain a fresh surface for the evaporation of Ti(5 nm)/Au(80 nm) at a base pressure of  $1 \times 10^{-8}$  mbar to form Ohmic contacts. After deposition of the Ohmic contacts, the MoS<sub>2</sub> is transferred *ex situ* to a thermal evaporator system equipped with an annealing stage (R-DEC) for the Schottky-contact deposition. First, the MoS<sub>2</sub> crystal is annealed at 350 °C for 2.5 h to improve the quality of the Ohmic contacts by removing physisorbed material at the interface or to promote an interface reaction of Ti with the MoS<sub>2</sub> surface, and to outgas physisorbed contaminants on the surface of the MoS<sub>2</sub> crystal. Next, Au(15 nm) is

thermally evaporated onto the clean surface of the MoS<sub>2</sub> crystal through a shadow mask at the rate of 0.2 Å/s at approximately 50 °C at a base pressure of  $1 \times 10^{-8}$  mbar. The larger circular Au devices are 500 μm in diameter and the smaller circular Au devices are 250 μm in diameter, while the rectangular Ti/Au Ohmic contacts on each side of the substrate are 0.7 × 7 mm<sup>2</sup>. Finally, the samples are transferred *ex situ* to an UHV Nanoprobe system (Omicron), which is an ultrahigh-vacuum (base pressure  $1 \times 10^{-10}$  mbar) four-probe STM system equipped with three standard STM probes for contacted *I-V* measurements, one atomic resolution capable STM probe and a Zeiss Gemini SEM imaging column for accurate positioning of the probes. The devices are measured without further annealing to prevent modification of the as-deposited interface. The manifestation of epitaxial Au(111) steps in the overgrowth Au cap layer (Fig. 6) provides an indication of good interface cleanliness and quality of this preparation method.

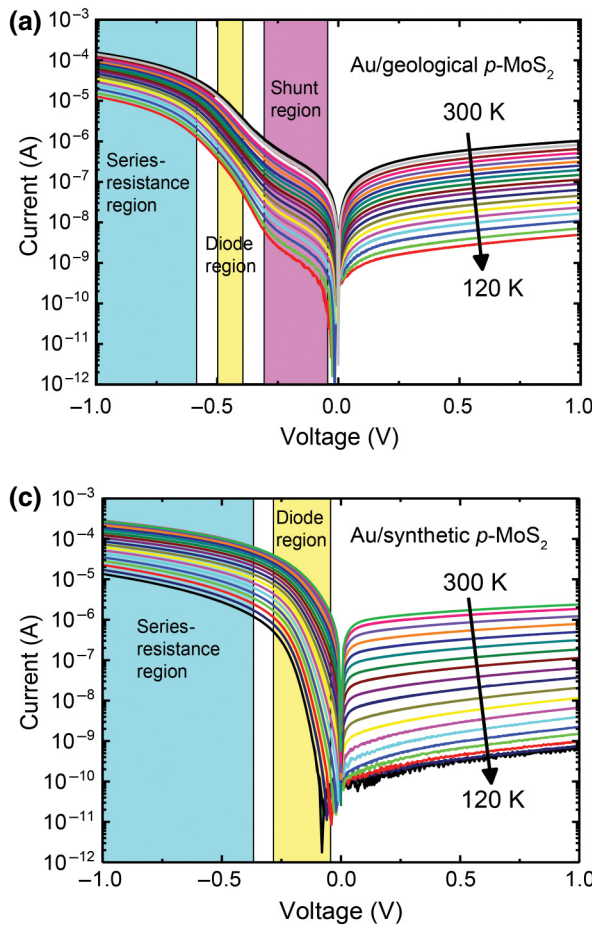
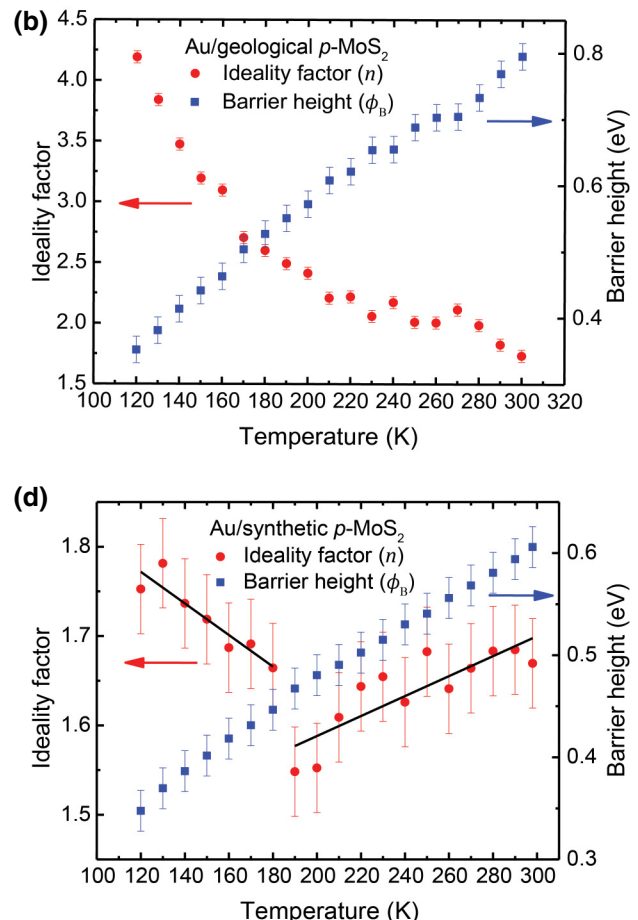


FIG. 2. (a) Temperature-dependent current-voltage (*I-V-T*) measurements of Au/geological *p*-MoS<sub>2</sub> from 300 K (room temperature) to 120 K. The device area is 0.196 mm<sup>2</sup>. (b) Plots of extracted diode parameters for the Au/geological MoS<sub>2</sub> Schottky diode against temperature. Ideality factor (red, left axis) and barrier height (blue, right axis). (c) Temperature-dependent current-voltage (*I-V-T*) measurements of Au/synthetic *p*-MoS<sub>2</sub> and (d) the extracted diode parameters for the Au/synthetic MoS<sub>2</sub> devices. Black lines are guides to the eye for showing two ideality-factor ranges. The error bars of  $n \pm 0.05$  and  $\phi \pm 0.02$  eV are estimated from the error of range of fit of Eq. (3) to Figs. 2(a) and 2(c).

## IV. RESULTS

### A. *I-V-T* measurements

Figure 2 shows the *I-V-T* measurements of Au/geological MoS<sub>2</sub> and the Au/synthetic MoS<sub>2</sub> Schottky diodes. From the *I-V-T* characteristics of the devices, we observe the typical rectifying behavior of a *p*-type Schottky diode with low leakage at positive bias and current turn on at negative biases and hence can conclude that our MoS<sub>2</sub> devices are *p* type. A shunt conduction pathway, which could arise from conduction through defective regions with lower resistance is present for the geological MoS<sub>2</sub> crystal. The synthetic MoS<sub>2</sub> device shows a typical diode *I-V* characteristic with low leakage under reverse bias, turn on at threshold followed by monatomic rise in *I*, with no defect-dominated shunt at low biases, from which we can conclude that the synthetic MoS<sub>2</sub> crystal is cleaner. The presence of a high series resistance complicates the analysis due to voltage drop across the series resistance,



but can be corrected using the Werner method [34] (Fig. 7). We fit all the individual  $I$ - $V$  curves to the standard ideality-factor-modified thermionic emission model [Eq. (3)], to extract the Schottky-barrier heights ( $\phi$ ) and ideality factors ( $n$ ) as a function of temperature and plot the extracted values for the geological device in Fig. 2(b) and the synthetic device in Fig. 2(d).  $A^{**} = 400\ 000 \text{ A m}^{-2} \text{ K}^{-2}$  is used as the theoretical effective Richardson constant of  $p$ -MoS<sub>2</sub> [35]. Fig. 2(b) shows that the temperature-dependent SBHs extracted from both MoS<sub>2</sub> substrates are inversely proportional to temperature and the ideality factors are proportional to temperature, similar to many reports in the literature. Furthermore, Fig. 2(d) shows two regimes where the ideality factor scales differently as a function of temperature. This behavior, where the ideality factor decreases as temperature decreases is contrary to that in typical devices where the ideality factor increases when temperature decreases, such as the geological MoS<sub>2</sub> sample [Fig. 2(b)]. This anomalous trend has been observed before by Aboelfotoh and Tu on the TiSi<sub>2</sub>/*n*-Si(100) Schottky barrier [36] and was later explained by Tung to arise from a convolution of charge transport through an inhomogeneous interface, which comprises of a mean Schottky-barrier height and a small number of low Schottky-barrier heights patches, where the mean Schottky-barrier height is only accessible at high enough temperatures [2,37], similar to method 4 of our analysis. Below 180 K, the usual trend of increasing ideality factor as temperature decreases returns. This can be explained by a freeze out of the mean Schottky-barrier region below 180 K and the device is dominated by the only the low barrier regions, and the trend returns to normal.

### 1. Methods 1, 2, and 3

To analyze the temperature dependence of the SBH and ideality factor, Fig. 3 shows the Richardson plots analyzed using methods 1, 2, and 3. By plotting the temperature-dependent Richardson plots, one can extract the effective Richardson constant and the SBH of the device from the gradient and the  $y$  intercept, respectively. However, the ideal Richardson plots and the ideality-factor modified Richardson plots [6,7] yield  $A^{**}$  values, which are orders of magnitude away from the theoretical values and expected values valid for the model, or give unrealistic SBH values. Table I shows the summary of the extracted  $\phi$  and  $A^{**}$  values using methods 1, 2, and 3. Method 1 gives the poorest fit to the experimental data, especially for low temperatures below approximately 180 K, where there is a large deviation from the linear fit. If we constrain the fits above 180 K, for the geological MoS<sub>2</sub> sample, we extract  $\phi_1 = 0.130 \text{ eV}$ ;  $A_1^{**} = 6.12 \times 10^{-6} \text{ A m}^{-2} \text{ K}^{-1}$  and for the synthetic MoS<sub>2</sub> sample  $\phi_1 = 0.216 \text{ eV}$ ;  $A_1^{**} = 0.198 \text{ A m}^{-2} \text{ K}^{-1}$ . While the  $\phi$  values are of a

TABLE I. Extracted Schottky-barrier heights and effective Richardson constants using methods 1, 2, and 3.

	Au/geological MoS <sub>2</sub>		Au/synthetic MoS <sub>2</sub>	
	$\phi$ (eV)	$A^{**}$ (A m <sup>-2</sup> K <sup>-1</sup> )	$\phi$ (eV)	$A^{**}$ (A m <sup>-2</sup> K <sup>-1</sup> )
<b>Method 1</b>	0.130	$6.12 \times 10^{-6}$	0.216	0.198
<b>Method 2</b>	0.884	5.43	0.334	0.105
<b>Method 3</b>	1.47	$3.15 \times 10^6$	0.369	$6.01 \times 10^{-6}$

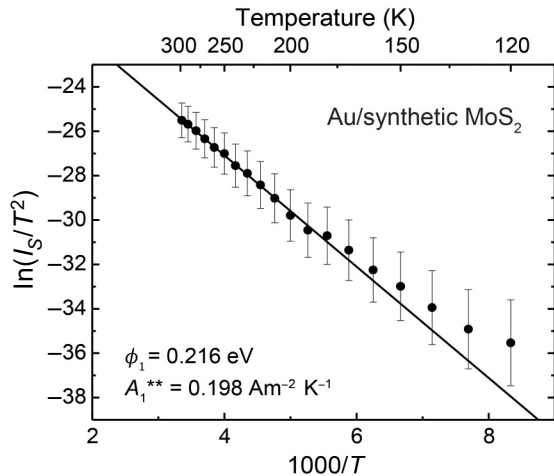
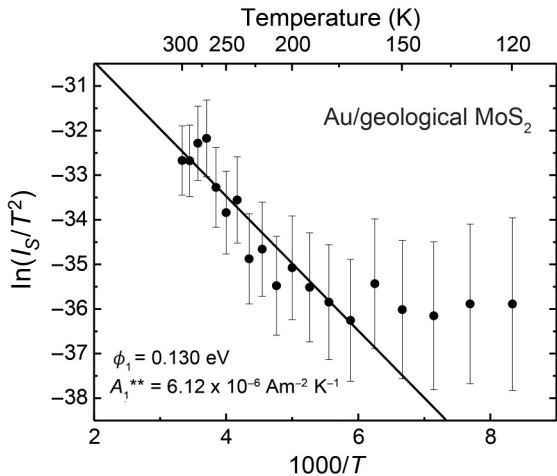
reasonable number, the  $A^{**}$  values are orders of magnitudes away from the theoretical value calculated from the effective mass of holes at the valance-band maxima of  $p$ -MoS<sub>2</sub> of  $A^{**} = 400\ 000 \text{ A m}^{-2} \text{ K}^{-2}$ . For method 2, we extract for the geological MoS<sub>2</sub> sample  $\phi_2 = 0.884 \text{ eV}$ ;  $A_2^{**} = 5.43 \text{ A m}^{-2} \text{ K}^{-1}$  and for the synthetic MoS<sub>2</sub> sample  $\phi_2 = 0.334 \text{ eV}$ ;  $A_2^{**} = 0.105 \text{ A m}^{-2} \text{ K}^{-1}$ . For method 3, for the geological MoS<sub>2</sub> sample  $\phi_3 = 1.47 \text{ eV}$ ;  $A_3^{**} = 3.15 \times 10^6 \text{ A m}^{-2} \text{ K}^{-1}$  and for the synthetic MoS<sub>2</sub> sample  $\phi_3 = 0.369 \text{ eV}$ ;  $A_3^{**} = 6.01 \times 10^{-6} \text{ A m}^{-2} \text{ K}^{-1}$ . For methods 2 and 3, although a linear fit can be obtained, and reasonable numbers can sometimes be extracted (method 3 yields an unreasonable SBH larger than the band gap of MoS<sub>2</sub> for the geological MoS<sub>2</sub> sample), the  $A^{**}$  values still do not match with the theoretical values and are varying over orders of magnitudes. It is important to note that for the synthetic MoS<sub>2</sub> sample, although methods 1, 2, and 3 give SBH of about 0.3 eV, the  $A^{**}$  values are incorrect over orders of magnitudes. Hence, we can conclude that it is useful to consider both the SBH and the  $A^{**}$  values together and that these models are inadequate, and a better model is required to explain the data.

### 2. Method 4

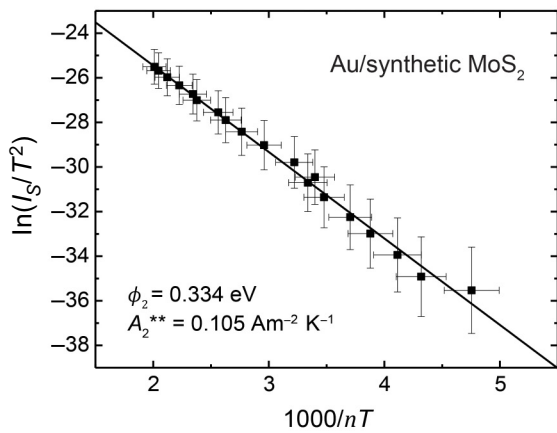
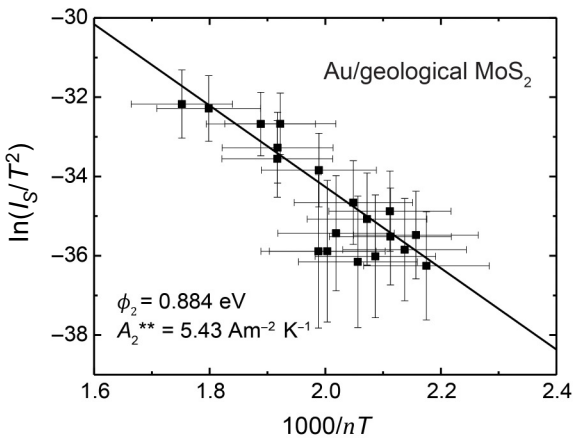
To further analyze the temperature dependence of the SBH, we use the inhomogeneous Gaussian-distributed Schottky-barrier height model proposed by Werner and Gütter [4], which is given by Eq. (8). Plotting  $\phi^{\text{app}}$  against  $q/2kT$  in Fig. 4 shows the presence of two different regimes where the two diode parameters dominate.

(a) *Geological MoS<sub>2</sub>* Fitting Eq. (8) to Fig. 4(a) shows that at temperatures above  $195 \pm 5 \text{ K}$ ,  $\Phi_4^{B1} = 0.88 \pm 0.10 \text{ eV}$  dominates the device performance while at temperatures below  $195 \pm 5 \text{ K}$ ,  $\Phi_4^{B2} = 1.18 \pm 0.14 \text{ eV}$  dominates the device performance. The Gaussian standard deviations ( $\sigma$ ) extracted from Fig. 4(a) are then used to correct for the Gaussian-distributed SBH to obtain the Gaussian-corrected Richardson plots [Fig. 4(c)]. Fitting Eq. (9) to the experimental data in the respective temperature regime in Fig. 4(c), the mean SBH values obtained from the corrected Richardson plots of  $\Phi_4^{B1} = 0.88 \pm 0.10 \text{ eV}$  and  $\Phi_4^{B2} = 1.18 \pm 0.14 \text{ eV}$  are an excellent

## (a) Method 1



## (b) Method 2



## (c) Method 3

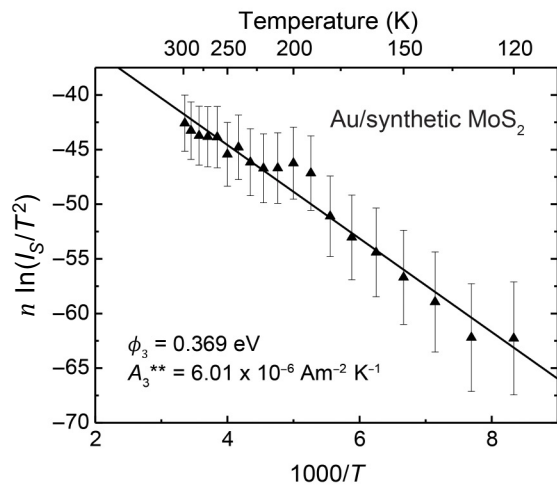
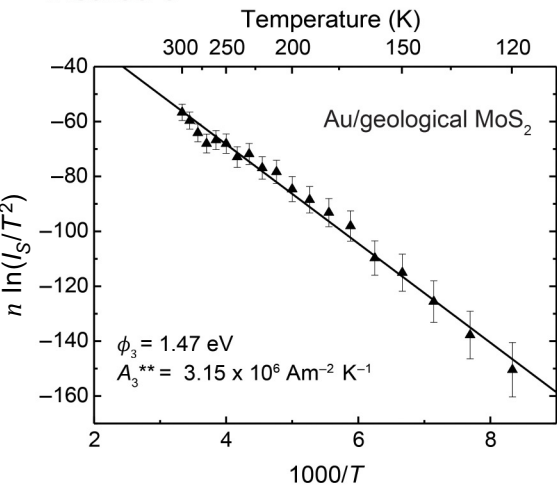


FIG. 3. Richardson plots and their ideality-factor-modified Richardson plots variants for the Au/geological MoS<sub>2</sub> (left column) and the Au/synthetic MoS<sub>2</sub> (right column). (a) Method 1: standard Richardson plot  $\ln(I_s/T^2)$  against  $1/T$ . (b) Method 2: modified  $\ln(I_s/T^2)$  against  $1/nT$  and (c) Method 3: modified  $n \ln(I_s/T^2)$  against  $1/T$ . Error bars are estimated with  $\phi \pm 0.02$  eV and  $n \pm 0.05$  from fitting errors to extract SBH and  $n$ .

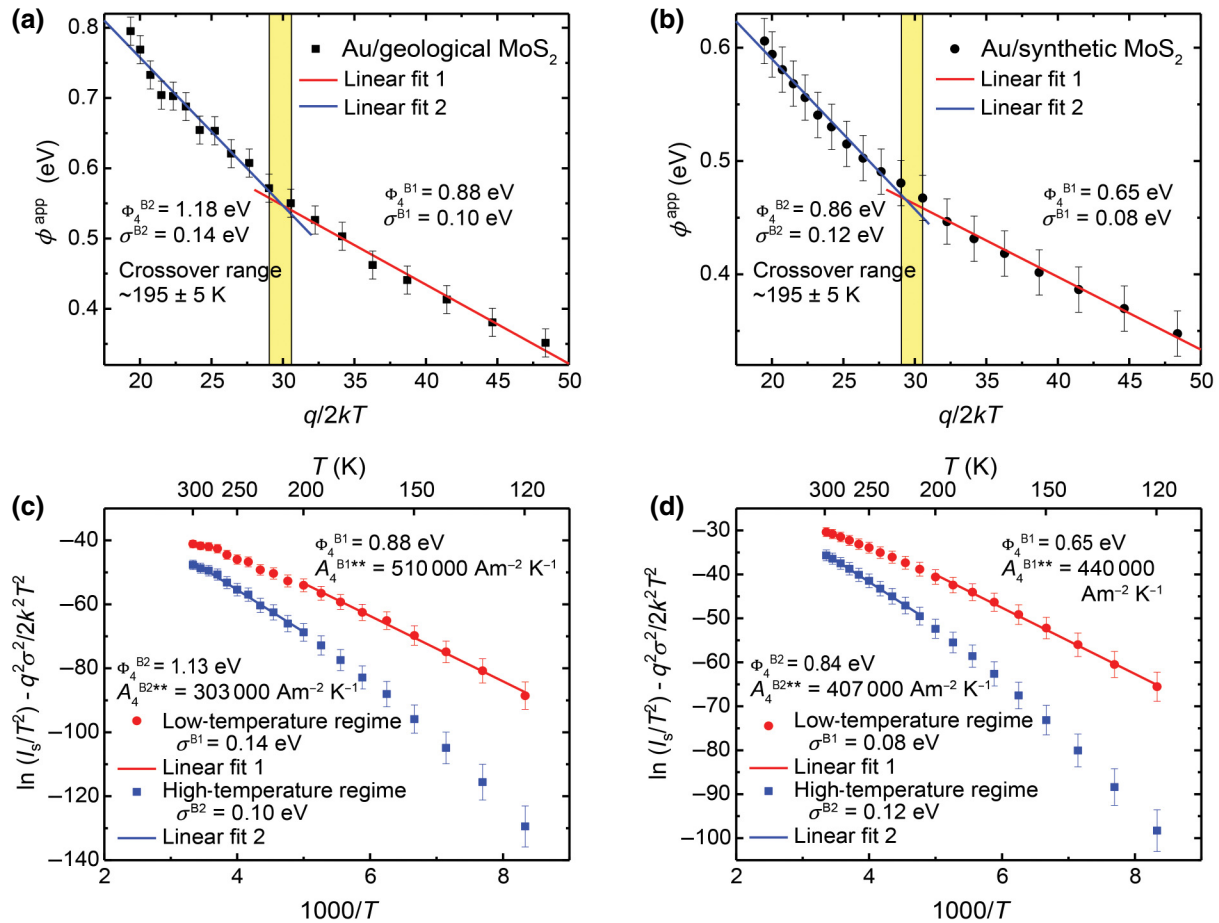


FIG. 4. (a) Double Gaussian plot of  $\phi_{\text{app}} \pm$  against  $q/2kT$  for the Au/geological MoS<sub>2</sub> crystal and (b) the Au/synthetic MoS<sub>2</sub> crystal. The solid lines are linear fits to Eq. (8) to obtain the mean Schottky-barrier height  $\Phi$  and the standard deviation  $\sigma$  of the Gaussian distribution. (c) Modified Richardson plot for the Au/geological MoS<sub>2</sub> crystal and (d) Au/synthetic MoS<sub>2</sub> crystal. The two plots are corrected with the  $\sigma$  of the Gaussian distributions in their respective temperature regimes. Linear fits to Eq. (9) give the  $\Phi_4$  from the gradient of the fit and  $A_4^{**}$  from the intercept.

match with the values obtained in Fig. 4(a),  $\Phi_4^{B1} = 0.88 \pm 0.10 \text{ eV}$  and  $\Phi_4^{B2} = 1.17 \pm 0.14 \text{ eV}$ . The average Richardson constants extracted from the Gaussian-corrected Richardson plot of  $A_4^{**} = 406\,000 \pm 145\,000 \text{ A m}^{-2} \text{ K}^{-1}$  is in good agreement with theoretical quantum-corrected value of  $A^{**} = 400\,000 \text{ A m}^{-2} \text{ K}^{-1}$  [12,13], validating the feasibility of this method.

(b) *Synthetic flux grown MoS<sub>2</sub>* Similarly for the synthetic MoS<sub>2</sub> crystal, Fig. 4(b) shows that at high temperatures above  $195 \pm 5 \text{ K}$ , the  $\Phi_4^{B1} = 0.86 \pm 0.12 \text{ eV}$  dominates the device performance while at low temperatures, the  $\Phi_4^{B2} = 0.65 \pm 0.08 \text{ eV}$  dominates the device performance. Plotting the Gaussian-modified Richardson plot in Fig. 4(d) reveals a similar behavior as the geological MoS<sub>2</sub> sample. The mean SBH values extracted from the Richardson plots of  $\Phi_4^{B1} = 0.84 \pm 0.12 \text{ eV}$  and  $\Phi_4^{B2} = 0.65 \pm 0.08 \text{ eV}$  are an excellent match with the

values obtained in Fig. 4(b) with a similar temperature crossover range of  $195 \pm 5 \text{ K}$ . Furthermore, the average  $A_4^{**}$  extracted from the synthetic MoS<sub>2</sub> of  $424\,000 \pm 23\,000 \text{ A m}^{-2} \text{ K}^{-1}$  is in excellent agreement with the  $A_4^{**}$  of geological MoS<sub>2</sub> of  $406\,000 \pm 145\,000 \text{ A m}^{-2} \text{ K}^{-1}$ , and again with the theoretically derived values of  $400\,000 \text{ A m}^{-2} \text{ K}^{-2}$ . These results provide crucial support for the validity of using the Gaussian-modified SBH model in our samples.

## B. BHEM

To further verify the presence of a Gaussian-distributed SBH, we use ballistic hole emission microscopy (BHEM), which is a nanoscale technique based on scanning tunneling microscopy (STM) to measure the local SBH of the interface for the two different MoS<sub>2</sub> crystals. In a typical BHEM experiment, holes are injected into the Au layer from the STM tip by applying a positive tip bias ( $V_T$ ), while the Au layer and the MoS<sub>2</sub> substrate are grounded

[Fig. 1(a)]. Some of the holes travel through the thin Au layer (15 nm) unscattered (the ballistic holes) to reach the metal-semiconductor interface and are collected as the BHEM current ( $I_B$ ) at the Ti/Au Ohmic contact if they have enough energy to overcome the Schottky barrier and fulfil the momentum conservation rules [9,38]. To obtain the local Schottky-barrier height ( $\phi_{\text{BHEM}}$ ), we use the spectroscopy mode by holding the STM tip at a fixed ( $x, y$ ) position with the tunnelling current ( $I_T$ ) feedback loop kept on, and collect the BHEM current ( $I_B$ ) as a function of the bias ( $V_T$ ) applied between the tip and the Au layer. We normalize the transmission ( $R$ ) of the interface by taking the ratio of the  $I_B$  and the  $I_T$  and plotted this ratio against the tip bias to obtain the BHEM spectra [Eq. (10)], which is a function of the transmission of the interface to the energy of the electrons. In addition to the main advantage of the nanoscale spatial resolution in BHEM, the *zero bias SBH* (i.e., the equilibrium band alignment) can be measured and visualized directly without having to assume a transport model. For one dataset, we collect approximately 800 BHEM spectra over a 200 nm by 200 nm area and extract the local SBH by fitting an individual spectrum to the Prietsch-Ludeke (PL) model [Eq. (10)] in the range of 0.3 to 1.3 V, about 0.4 V above the SBH [38,39] (Fig. 8). A statistical  $R^2$  value is used to select the quality of fit of the spectra, for  $R^2 < 0.6$ , the spectra are rejected. Usually, these rejected spectra have either no threshold, or display sudden current jumps due to equipment instability.

$$\frac{I_B}{I_T} = R \frac{(\phi_{\text{BHEM}} - eV)^{5/2}}{eV}. \quad (10)$$

We collected a few datasets over a few different locations on the same sample and Fig. 5 shows a representative statistical spread of the local SBH for the two crystals taken from one of the datasets. For the Au/geological MoS<sub>2</sub> device, we obtain the local  $\phi_{\text{BHEM}} = 0.86 \pm 0.02$  eV, while for the Au/synthetic MoS<sub>2</sub>, we obtain a  $\phi_{\text{BHEM}} = 0.89 \pm 0.02$  eV. The nanoscale SBH for both the geological and synthetic Au/MoS<sub>2</sub> samples are similar, affirming that although the crystal quality is likely to be different, the pristine SBH is similar in value and a Gaussian distribution with  $\sigma = 0.02$  eV is present for both samples.

Table II shows the summary of the Schottky-barrier heights obtained for the Au/geological *p*-MoS<sub>2</sub> and Au/synthetic *p*-MoS<sub>2</sub> using *I-V-T* measurements and BHEM. We propose that the pristine zero-bias SBH for the Au/*p*-MoS<sub>2</sub> interface is approximately 0.86 eV as this value is obtained across complementary techniques and different MoS<sub>2</sub> sources. There is at least one defective region present in each sample. We generalize these defects into two regimes, defect 1 is a lower-barrier region, which is present in both the geological and synthetic MoS<sub>2</sub> crystals. The density of defect 1 in the geological crystal could be higher, and thus exists as a shunt region. We propose

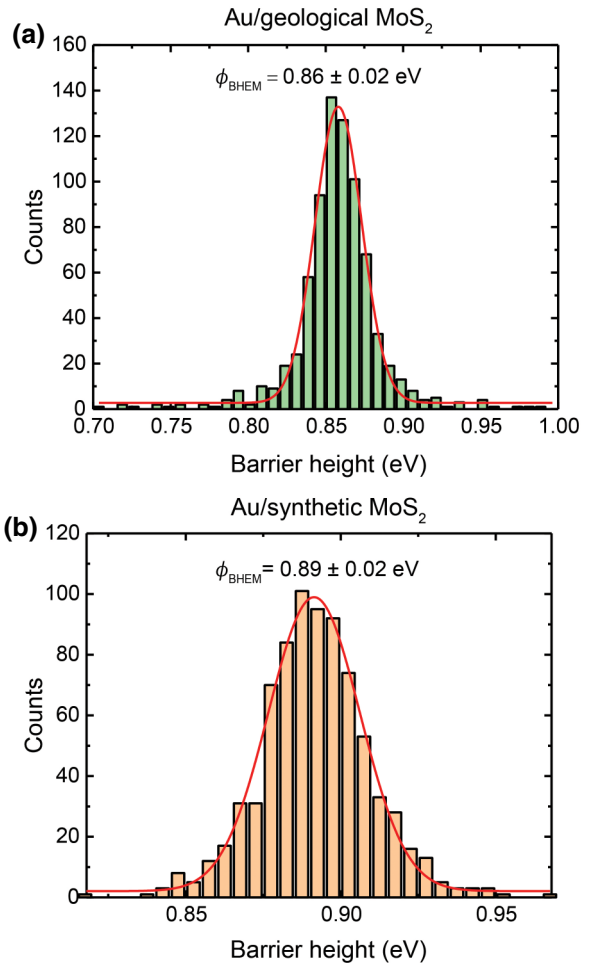


FIG. 5. Statistical plot of the Schottky-barrier height measured at 120 K for (a) Au(15 nm)/geological MoS<sub>2</sub>,  $\phi_{\text{BHEM}} = 0.86 \pm 0.02$  eV, 770 data points. (b) Au(15 nm)/synthetic MoS<sub>2</sub>,  $\phi_{\text{BHEM}} = 0.89 \pm 0.02$ , 797 data points.

that the convolution of the lower-barrier defect with the pristine SBH can explain the spread of SBH values in the literature as the extracted numbers will differ across different samples and measurement temperatures. Defect 2 is associated with the higher-barrier region possibly by doping, only detected in the geological MoS<sub>2</sub> crystal, typically not a dominating effect in the *I-V* measurements due to the exponential relationship of  $I$  to  $\phi$  in the thermionic emission model.

From Table II, we can conclude that the nanoscale SBH measured using BHEM and macroscale SBH determined using *I-V-T* measurements are in excellent agreement. Standard deviations of the macroscale SBH are one order of magnitude larger than the nanoscale SBH. This can be explained by the nonuniform area of the measurement. *I-V-T* measurements give a weighted average of the SBH across the whole device area (0.196 mm<sup>2</sup>), which includes contributions from defects such as step edges, impurities, etc. while the nanoscale SBH has a resolution of a few

TABLE II. Schottky-barrier heights of Au/geological *p*-MoS<sub>2</sub> and Au/synthetic *p*-MoS<sub>2</sub> measured using temperature-dependent current-voltage (*I-V-T*) measurements and ballistic hole emission microscopy (BHEM). Defects 1 and 2 denote the two Schottky-barrier heights obtained from the double-Gaussian distribution model of Schottky-barrier heights that could arise from different kind of defects.

Origin of SBH	MoS <sub>2</sub> /geological MoS <sub>2</sub>		MoS <sub>2</sub> /synthetic MoS <sub>2</sub>	
	$\Phi$ (eV)	$A^{**}$ (A m <sup>-2</sup> K <sup>-1</sup> )	$\Phi$ (eV)	$A^{**}$ (A m <sup>-2</sup> K <sup>-1</sup> )
Defect 1	Not detected <sup>a</sup>	—	$0.64 \pm 0.08$	440 000
Pristine	$0.88 \pm 0.14$	509 000	$0.84 \pm 0.12$	407 000
Defect 2	$1.17 \pm 0.10$	303 000	—	—
BEEM	$0.86 \pm 0.02$	—	$0.89 \pm 0.02$	—

<sup>a</sup>Shunt resistance  $R_p = 900$  k $\Omega$  dominates.

nanometers, which measures largely the pristine SBH at the interface. We did not detect the presence of atomic scale defects in BHEM imaging and spectroscopy, i.e., the scanned areas show a single Gaussian-distributed SBH over hundreds of nanometers. Point defects such as vacancies are not resolved in BHEM measurements likely due to the pinch-off effect [40], where a point defect smaller than the depletion width of the semiconductor will be pinched off, but they are expected to be present and a cluster of these vacancies can cause a saddle point [1,2,37] and may be convoluted in the Gaussian-distributed potential fluctuation of the SBH, or provide a doping effect [41]. This means that a low area density of defects dominates the device in macroscale *I-V-T* measurements and mask the pristine interface typically measured in nanoscale BEEM.

## V. DISCUSSION

The different *I-V* behaviors of geological and synthetic flux grown MoS<sub>2</sub> crystals point to the significance of obtaining high-quality crystals for device fabrication. Devices fabricated from the synthetic flux grown crystal show more uniform Schottky-diode performances than geological MoS<sub>2</sub> as the geological crystal contains many impurities that unintentionally dope the crystal. Although some of the best reported devices are made using geological crystals, the high density of contamination in geological crystals results in poor reproducibility and reliability in the electronic properties of 2D devices. It is difficult to differentiate intrinsic material properties from unwanted dopant effects, which can explain the spread of behaviors of devices in the literature. Addou *et al.* recently studied the surface of geological MoS<sub>2</sub> using STM and showed that the surface of the crystal shows huge variation across the same sample due to impurities [27,28], which suggests that these impurities are significant contributors to the electrical behavior of the devices [29]. We also observe similar

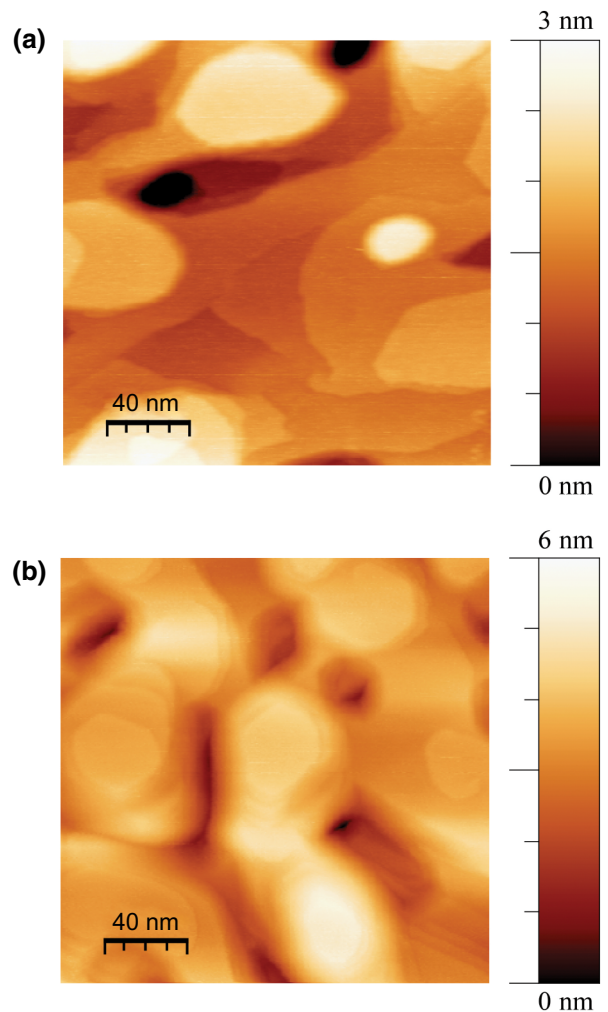


FIG. 6. STM images of the Au/MoS<sub>2</sub> images at 1.5 V tip bias showing the epitaxial Au overgrowth layer. (a) Au/geological MoS<sub>2</sub>, (b) Au/synthetic MoS<sub>2</sub>.

defects and impurities in our samples using STM imaging (Fig. 9), but similar to their analysis, we are unable to identify the chemical composition of the defects in STM and ballistic electron emission microscopy (BEEM) and *I-V* measurements as these techniques do not have chemical sensitivity. We show that the double-Gaussian model proposed in this paper can be used to deconvolute the defective SBH from the pristine SBH. This method is also useful for research on engineering Ohmic contacts to these materials.

Our MoS<sub>2</sub> crystals are *p*-type crystals. In the recent literature, most MoS<sub>2</sub> crystals reported are *n*-type semiconductors [42–47]. However, early reports have noted that some geological samples are intrinsically *p* type [48–50] and for synthetic crystals, depending on the growth method, the TMDC crystals can be unintentionally doped *n* type or *p* type due to doping from the chemical-transport agent or impurity inclusion [51,52]. The Gaussian-distributed

model should also work for *n*-type MoS<sub>2</sub> and other TMDCs. Cook *et al.* studied the *n*-type MoS<sub>2</sub> using BEEM and they obtained the Au/*n*-MoS<sub>2</sub> SBH of  $0.48 \pm 0.02$  eV for 16 nm Au layers [53]. Our *p*-type SBH and their *n*-type SBH for approximately 15 nm Au layer sum up to approximately the band gap of bulk MoS<sub>2</sub> (approximately 1.34 eV), which provides a useful consistency check, and suggests an unpinned Fermi level. We do not detect any signature of strain in our devices at the limit of resolution of our Raman spectrograph (Fig. 10), suggesting that the strain did not play a significant role in our measurements. Figure 6 shows the STM image of epitaxial Au films on MoS<sub>2</sub> grown using a slow deposition method, which is an indirect evidence of a clean abrupt interface Au/MoS<sub>2</sub> [18,20]. Our results lend support to the presence of an unpinned Fermi level for a well-prepared van der Waal's Au/MoS<sub>2</sub> interface that is deposited slowly (approximately 0.2 Å/s), consistent with a few recent reports [19,20], and an old photoemission study [54].

Our BHEM results seem to point to the presence of low elastic scattering, as our SBH distribution can be well modeled by a single symmetric Gaussian distribution. This is consistent with the results of Nolting *et al.*, where a single symmetric Gaussian distribution can be well fit to a well-prepared abrupt metal-semiconductor interface without any interface reactions [55–57]. We also note that the Gaussian-distributed SBH analysis method we propose in this paper has been applied also to monolayer MoS<sub>2</sub> devices [58]. In their report, Moon *et al.* analyzed the top and edge contact of Au/MoS<sub>2</sub> *n*-type FET devices using the Gaussian-distribution model at different gate bias. They observe the top contact has a larger SBH and larger  $\sigma$ , showing more inhomogeneity than in the edge contact, which has a lower SBH and lower  $\sigma$ . However, they did not use the Gaussian-corrected Richardson plot, but they indicated that the standard Richardson plot is not valid due to an observed temperature dependence of the SBH. Our method of analysis can be used to bridge the gap between real 2D devices and theoretically proposed models [24] by deconvoluting SBH inhomogeneity from intrinsic material transport behaviors.

## VI. CONCLUSION

We show that the presence of inhomogeneities at the metal-semiconductor interface should be considered in the extraction of device parameters. The analysis of *I-V-T* measurements without considering the Gaussian distribution of Schottky-barrier heights results in an apparent Schottky-barrier height ( $\phi^{\text{app}}$ ), which is not reflecting the intrinsic behavior of the interface, but the convoluted effects of low barrier regions (defects), pristine regions, and temperature. Using the Gaussian-modified Richardson plots, reliable mean SBH ( $\Phi$ ) can be extracted, and the

extracted effective Richardson constants ( $A^{**}$ ) are close to the theoretical calculated Richardson constants. We report an experimentally measured value of  $A^{**} = 415\,000 \pm 85\,000$  A m<sup>-2</sup> K<sup>-1</sup> based on our averaged  $A^{**}$  measurements in contrast to  $A^{**} = 745\,000$  A m<sup>-2</sup> K<sup>-1</sup> typically assumed for *p*-type MoS<sub>2</sub> devices and the Au/*p*-MoS<sub>2</sub> SBH of approximately  $0.86 \pm 0.14$  eV obtained as an averaged value across two different samples and complementary techniques.

We used BHEM, which is a more tedious but direct method to measure the zero-bias SBH without the need to rely on the validity of temperature-dependent models, and to experimentally validate the significance of including a Gaussian-distributed SBH at the nanoscale in conventional *I-V-T* analysis. Our results provide the basic framework for extracting the pristine SBH from temperature-dependent *I-V* data and demonstrate that with careful use of the dual parameter ( $A^{**} + \text{SBH}$ ) analysis, we avoid obtaining unphysical numbers that are counterproductive for understanding such interfaces. This implies that the *I-V-T* analysis can yield useful insights on the SB inhomogeneities even though it might be a macroscale measurement.

## ACKNOWLEDGMENTS

This research is supported by the Agency for Science, Technology and Research (A\*STAR) under its A\*STAR QTE Grant No. A1685b0005 and the A\*STAR Pharos Grant No. 1527000016.

## APPENDIX A: WERNER METHOD

The Werner method is used to correct for the high series resistance present in the *I-V-T* curves of our Au/MoS<sub>2</sub> diodes [34]. Under forward bias and with series-resistance contribution, the voltage across the diode,  $V_D = V - IR_s$  and  $V_D \gg kT$ , the thermionic emission current [Eq. (A1)] is given by the simplified form:

$$I_D = I_S \exp \left[ \frac{q(V - IR_s)}{nkT} \right], \quad (\text{A1})$$

where  $I_D$  is the thermionic diode current. Differentiating Eq. (A1) gives the small signal conductance  $G = dI_D/dV$  and one obtains

$$\frac{G}{I_D} = \frac{q}{nkT} (1 - GR_s). \quad (\text{A2})$$

Werner showed that by plotting  $G/I_D$  against  $G$ , named hereafter as the Werner plot, will give a straight line with a *y*-axis intercept of  $q/nkT$ , where  $n$  can be extracted, and the *x* axis gives the intercept of  $1/R_s$ .

Figure 7 shows the representative experimental Werner plot for our Au/MoS<sub>2</sub> diode at 300, 250, and 200 K from which their respective  $n$  and  $R_s$  values can be extracted

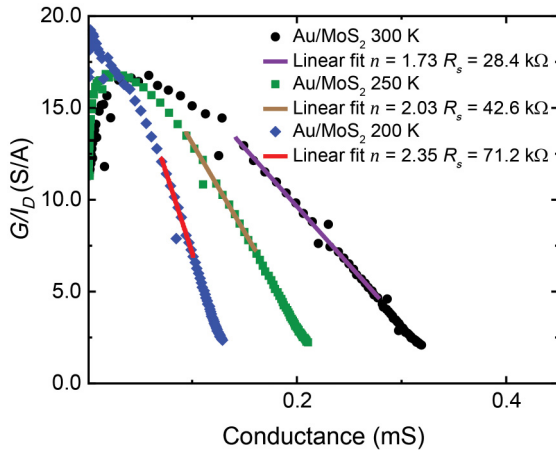


FIG. 7. Experimental Werner plot for the Au/geological MoS<sub>2</sub> diode at 300, 250, and 200 K. The linear fit to the data according to Eq. (A2) yields  $n = 1.73$  and  $R_s = 28.4\text{ k}\Omega$  at 300 K,  $n = 2.03$  and  $R_s = 42.6\text{ k}\Omega$  at 250 K and  $n = 2.35$  and  $R_s = 71.2\text{ k}\Omega$  at 200 K.

from the  $y$  intercept and  $x$  intercept, respectively. After extracting the  $R_s$  and  $n$  from the Werner plots, the effect of  $R_s$  on the bias voltage can be corrected by subtracting the voltage drop across the series resistance by Kirchhoff's law using  $V_D = V - IR_s$ . From the  $R_s$ -corrected  $I$ - $V$  plots, we fit the standard thermionic emission model [Eq. (3)] in the linear diode regime to obtain the Schottky-barrier height and the ideality factor. The ideality factors extracted from the Werner plots and the corrected  $I$ - $V$  plots are within 10% error, validating the Werner method.

## APPENDIX B: PRIETSCH-LUDEKE MODEL

To fit the BHEM spectra, we consider both the Bell-Kaiser (BK) [10,23] and Prietsch-Ludeke (PL) [39] models. The difference between the two models are in the exponent  $n$  of Eq. (B1). The BK model has  $n = 2$  while the PL model is  $n = 5/2$ . The additional 1/2 power for the PL model comes from the inclusion of quantum-mechanical reflection at the metal-semiconductor interface.

$$\frac{I_B}{I_T} = R \frac{(\phi_B - eV)^n}{eV}. \quad (\text{B1})$$

Figure 8 shows that for our experimental data, the PL model fits better than the BK model in the fitting range of 0.3 to 1.3 V, about 0.4 V above the SBH. Therefore, the PL model is used in our analysis.

## APPENDIX C: DEFECT IMAGING USING SCANNING TUNNELING MICROSCOPY

We also see defects that were previously reported by Addou *et al.* in our geological MoS<sub>2</sub> samples [27,28]. Figure 9 shows the STM images that we obtain from our

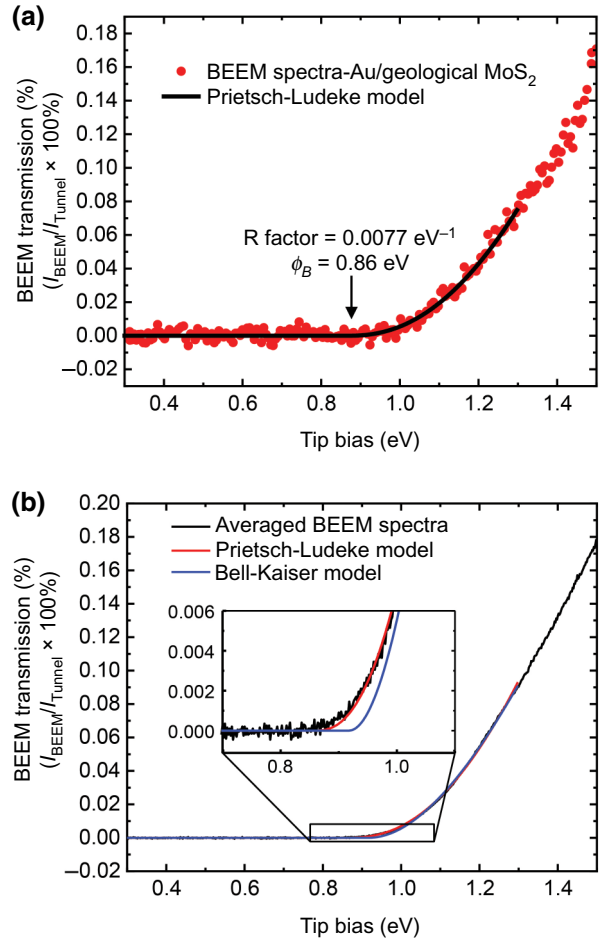


FIG. 8. (a) Single representative BEEM spectrum of Au/geological MoS<sub>2</sub>, fitting the PL model yields  $\phi_B = 0.86\text{ eV}$   $R$  factor =  $0.0077\text{ eV}^{-1}$  (b) Averaged BEEM spectrum of Au/geological MoS<sub>2</sub> (674 points) to increase the signal-to-noise ratio. Inset shows an enlargement of the threshold region, the spectrum fits better to the PL model.

MoS<sub>2</sub> samples. Figures 9(a) and 9(b) show the same region scanned at positive and negative biases, respectively. We observe a contrast inversion of some defects where two of the dark defects under positive bias [Figure 9(a)] appears bright under negative-bias conditions [Figure 9(b)] similar to those defects seen by Addou *et al.*, where they attributed these to metallic impurity clusters present on the surface of the MoS<sub>2</sub> crystals. A local depression is also detected in our sample, similar to Addou *et al.*, which could be sulfur vacancies or subsurface sulfur vacancies. These defects could cause the electronic inhomogeneities discussed in the main text of the paper.

## APPENDIX D: STRAIN ANALYSIS USING RAMAN SPECTROSCOPY

To study the effect of strain at our Au/MoS<sub>2</sub> interface, we use Raman spectroscopy to compare the relative shifts

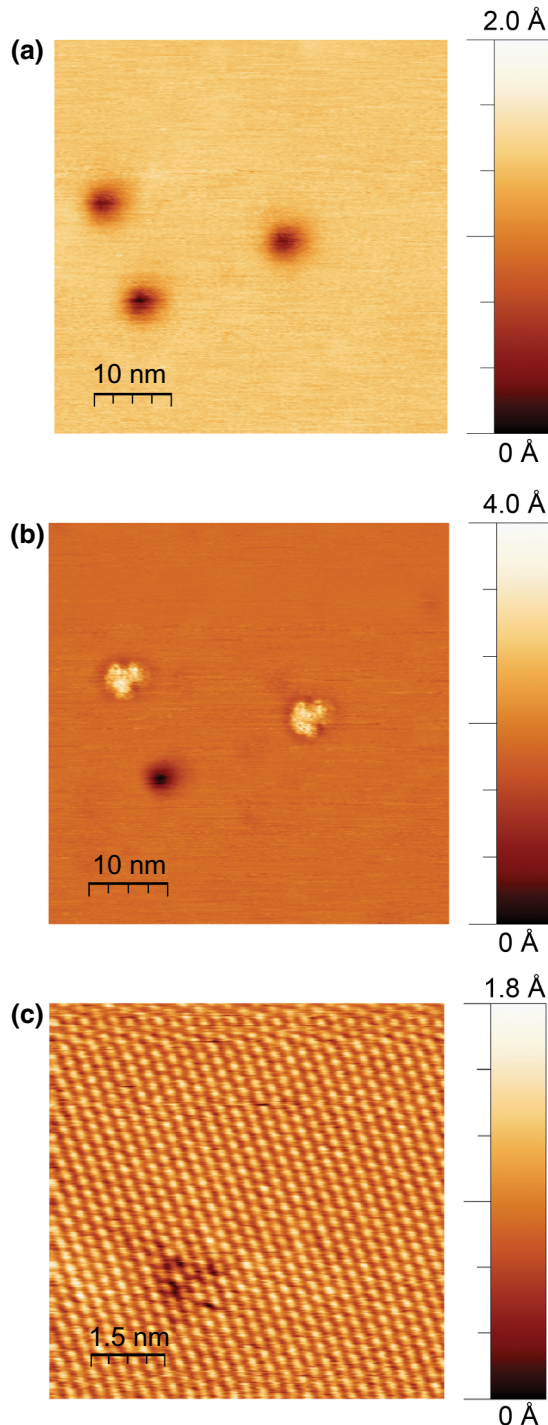


FIG. 9. Scanning tunneling microscopy images of (a) the MoS<sub>2</sub> surface, metallic clusterlike impurities observed at +0.6 V, 2 nA. (b) same area, but at -0.6 V, 2 nA, notice the contrast inversions (c) local depressions observed at -0.6 V, 50 pA.

of the vibrational modes. Figure 10 shows the Raman spectrum obtained on our Au/synthetic MoS<sub>2</sub> device using a 532-nm laser at 120 K using a liquid-nitrogen flow stage (Linkam). No shift of the Raman peaks is detected when we collect the spectrum on the bare MoS<sub>2</sub> surface and on

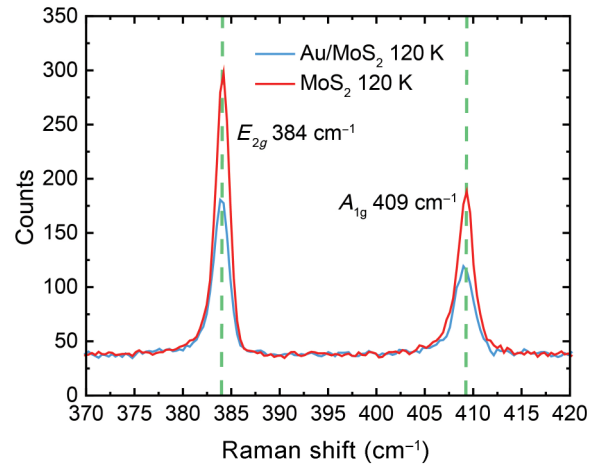


FIG.10. Raman spectrum collected on the Au/MoS<sub>2</sub> surface and the bare MoS<sub>2</sub> surface at 120 K using liquid nitrogen cooling and 532-nm laser excitation.

the Au/MoS<sub>2</sub> although a decrease in peak intensity can be detected due to attenuation by the 15-nm Au layer. The Raman peaks all match within 0.2 cm<sup>-1</sup>, which is the resolution limit of our Raman spectrometer. Hence, we conclude that we do not detect any strain in our Au/MoS<sub>2</sub> devices.

- [1] R. T. Tung, The physics and chemistry of the Schottky barrier height, *Appl. Phys. Rev.* **1**, 011304 (2014).
- [2] R. T. Tung, Electron transport at metal-semiconductor interfaces: General theory, *Phys. Rev. B* **45**, 13509 (1992).
- [3] J. H. Werner and H. H. Gütter, Transport properties of inhomogeneous Schottky Contacts, *Phys. Scr.* **1991**, 258 (1991).
- [4] J. H. Werner and H. H. Gütter, Barrier inhomogeneities at Schottky contacts, *J. Appl. Phys.* **69**, 1522 (1991).
- [5] S. M. Sze and K. K. Ng, *Physics of Semiconductor Devices*, 3rd Ed (John Wiley & Sons, Inc, Hoboken, NJ, USA, 2006).
- [6] A. S. Bhuiyan, A. Martinez, and D. Esteve, A new Richardson plot for non-ideal Schottky diodes, *Thin Solid Films* **161**, 93 (1988).
- [7] R. Hackam and P. Harrop, Temperature dependence of the Schottky barrier height in gallium arsenide, *Solid State Commun.* **11**, 669 (1972).
- [8] R. Hackam and P. Harrop, Electrical properties of nickel-low-doped n-type gallium arsenide Schottky-barrier diodes, *IEEE Trans. Electron Devices* **19**, 1231 (1972).
- [9] L. D. Bell, New electron and hole spectroscopies based on ballistic electron emission microscopy, *J. Vac. Sci. Technol. B* **9**, 594 (1991).
- [10] W. J. Kaiser and L. D. Bell, Direct Investigation of Sub-surface Interface Electronic Structure by Ballistic-Electron-Emission Microscopy, *Phys. Rev. Lett.* **60**, 1406 (1988).
- [11] L. D. Bell, M. H. Hecht, W. J. Kaiser, and L. C. Davis, Direct Spectroscopy of Electron and Hole Scattering, *Phys. Rev. Lett.* **64**, 2679 (1990).

- [12] A. M. Cowley and S. M. Sze, Surface states and barrier height of metal-semiconductor systems, *J. Appl. Phys.* **36**, 3212 (1965).
- [13] H. Peelaers and C. G. Van De Walle, Effects of strain on band structure and effective masses in MoS<sub>2</sub>, *Phys. Rev. B* **86**, 241401 (2012).
- [14] C. R. Crowell and S. M. Sze, Current transport in metal-semiconductor barriers, *Solid. State. Electron.* **9**, 1035 (1966).
- [15] F. A. Padovani and R. Stratton, Field and thermionic-field emission in schottky barriers, *Solid State Electron.* **9**, 695 (1966).
- [16] D. Qiu and E. K. Kim, Electrically tunable and negative Schottky barriers in multi-layered graphene/MoS<sub>2</sub> heterostructured transistors, *Sci. Rep.* **5**, 13743 (2015).
- [17] M. Tao, D. Udeshi, S. Agarwal, R. Kolappan, Y. Xu, E. Maldonado, and W. P. Kirk, Se-Passivated Si(100) surface for low and negative Schottky barriers, *Ext. Abstr. Fourth Int. Work. Junction Technol. IWJT 2004* **4**, 119 (2004).
- [18] S. Nagashima and I. Otsuka, Surface topography of epitaxial Au(111) films deposited on MoS<sub>2</sub>, *J. Cryst. Growth* **146**, 266 (1995).
- [19] Y. Liu, J. Guo, E. Zhu, L. Liao, S. J. Lee, M. Ding, I. Shakir, V. Gambin, Y. Huang, and X. Duan, Approaching the Schottky-Mott limit in van der Waals metal-semiconductor junctions, *Nature* **557**, 696 (2018).
- [20] Y. Wang, J. C. Kim, R. J. Wu, J. Martinez, X. Song, J. Yang, F. Zhao, A. Mkhoyan, H. Y. Jeong, and M. Chhowalla, Van der Waals contacts between three-dimensional metals and two-dimensional semiconductors, *Nature* **568**, 70 (2019).
- [21] M. Moun and R. Singh, Barrier inhomogeneity in microscale Pt/MoS<sub>2</sub> Schottky barrier diode, *Semicond. Sci. Technol.* **33**, 125001 (2018).
- [22] A. Neetika, S. Kumar, A. Sanger, H. K. Chourasiya, A. Kumar, K. Asokan, R. Chandra, and V. K. Malik, Influence of barrier inhomogeneities on transport properties of Pt/MoS<sub>2</sub> Schottky barrier junction, *J. Alloys Compd.* **797**, 582 (2019).
- [23] L. D. Bell and W. J. Kaiser, Observation of Interface Band Structure by Ballistic-Electron-Emission Microscopy, *Phys. Rev. Lett.* **61**, 2368 (1988).
- [24] Y. S. Ang, H. Y. Yang, and L. K. Ang, Universal Scaling Laws in Schottky Heterostructures Based on Two-Dimensional Materials, *Phys. Rev. Lett.* **121**, 56802 (2018).
- [25] A. Allain, J. Kang, K. Banerjee, and A. Kis, Electrical contacts to two-dimensional semiconductors, *Nat. Mater.* **14**, 1195 (2015).
- [26] H. Liu, M. Si, Y. Deng, A. T. Neal, Y. Du, S. Najmaei, P. M. Ajayan, J. Lou, and P. D. Ye, Switching mechanism in single-layer molybdenum disulfide transistors: An insight into current flow across Schottky barriers, *ACS Nano* **8**, 1031 (2014).
- [27] R. Addou, L. Colombo, and R. M. Wallace, Surface defects on natural MoS<sub>2</sub>, *ACS Appl. Mater. Interfaces* **7**, 11921 (2015).
- [28] R. Addou, S. McDonnell, D. Barrera, Z. Guo, A. Azcatl, J. Wang, H. Zhu, C. L. Hinkle, M. Quevedo-Lopez, H. N. Alshareef, L. Colombo, J. W. P. Hsu, and R. M. Wallace, Impurities and electronic property variations of natural MoS<sub>2</sub> crystal surfaces, *ACS Nano* **9**, 9124 (2015).
- [29] S. McDonnell, R. Addou, C. Buie, R. M. Wallace, and C. L. Hinkle, Defect-Dominated doping and contact resistance in MoS<sub>2</sub>, *ACS Nano* **8**, 2880 (2014).
- [30] R. J. Archer and M. M. Atalla, Metals contacts on cleaved silicon surfaces, *Ann. N. Y. Acad. Sci.* **101**, 697 (1963).
- [31] R. T. Tung, J. P. Sullivan, and F. Schrey, On the inhomogeneity of Schottky barriers, *Mater. Sci. Eng. B* **14**, 266 (1992).
- [32] *Ward's Science*, “[https://www.wardsci.com/store/catalog/product.jsp?catalog\\_number=470178-584](https://www.wardsci.com/store/catalog/product.jsp?catalog_number=470178-584)”.
- [33] *2D Semiconductors*, “<https://www.2dsemiconductors.com/synthetic-molybdenum-disulfide-mos2>”.
- [34] J. H. Werner, Schottky barrier and Pn-Junction I/V plots — small signal evaluation, *Appl. Phys. A Solids Surfaces* **47**, 291 (1988).
- [35] This is calculated using the effective mass of holes at the valance band  $m^* = 0.62 m_0$  [13] using  $A^{**} = 4\pi qk_B^2 m^*/h^3$  and with a quantum correction factor of 0.5 following Cowley and Sze [12].
- [36] M. O. Aboelfotoh and K. N. Tu, Schottky-barrier heights of Ti and TiSi<sub>2</sub> on n-type and p-type Si(100), *Phys. Rev. B* **34**, 2311 (1986).
- [37] J. P. Sullivan, R. T. Tung, M. R. Pinto, and W. R. Graham, Electron transport of inhomogeneous Schottky barriers: A numerical study, *J. Appl. Phys.* **70**, 7403 (1991).
- [38] M. Prietsch, Ballistic-electron emission microscopy (BEEM): Studies of metal/semiconductor interfaces with nanometer resolution, *Phys. Rep.* **253**, 163 (1995).
- [39] M. Prietsch and R. Ludeke, Ballistic-Electron-Emission Microscopy and Spectroscopy of GaP(110)-Metal Interfaces, *Phys. Rev. Lett.* **66**, 2511 (1991).
- [40] A. Olbrich, J. Vancea, F. Kreupl, and H. Hoffmann, Potential pinch-off effect in inhomogeneous Au/Co/GaAs<sub>67</sub>P<sub>33</sub>(100)-Schottky contacts, *Appl. Phys. Lett.* **70**, 2559 (1997).
- [41] J. Yang, H. Kawai, C. P. Y. Wong, and K. E. J. Goh, Electrical doping effect of vacancies on monolayer MoS<sub>2</sub>, *J. Phys. Chem. C* **123**, 2933 (2019).
- [42] B. Radisavljevic, A. Radenovic, J. Brivio, V. Giacometti, and A. Kis, Single-layer MoS<sub>2</sub> transistors, *Nat. Nanotechnol.* **6**, 147 (2011).
- [43] C. H. Lee, G. H. Lee, A. M. Van Der Zande, W. Chen, Y. Li, M. Han, X. Cui, G. Arefe, C. Nuckolls, T. F. Heinz, J. Guo, J. Hone, and P. Kim, Atomically thin P-n junctions with van der Waals heterointerfaces, *Nat. Nanotechnol.* **9**, 676 (2014).
- [44] S. Das, H. Y. Chen, A. V. Penumatcha, and J. Appenzeller, High performance multilayer MoS<sub>2</sub> transistors with scandium contacts, *Nano Lett.* **13**, 100 (2013).
- [45] J. Suh, T. E. Park, D. Y. Lin, D. Fu, J. Park, H. J. Jung, Y. Chen, C. Ko, C. Jang, Y. Sun, R. Sinclair, J. Chang, S. Tongay, and J. Wu, Doping against the native propensity of MoS<sub>2</sub>: Degenerate hole doping by cation substitution, *Nano Lett.* **14**, 6976 (2014).
- [46] S. Kim, A. Konar, W.-S. Hwang, J. H. Lee, J. Lee, J. Yang, C. Jung, H. Kim, J.-B. Yoo, J.-Y. Choi, Y. W. Jin, S. Y. Lee, D. Jena, W. Choi, and K. Kim, High-mobility and Low-power thin-film transistors based on multilayer MoS<sub>2</sub> crystals, *Nat. Commun.* **3**, 1011 (2012).

- [47] B. Radisavljevic, M. B. Whitwick, and A. Kis, Integrated circuits and logic operations based on single-layer MoS<sub>2</sub>, *ACS Nano* **5**, 9934 (2011).
- [48] R. Mansfield and S. A. Salam, Electrical properties of molybdenite, *Proc. Phys. Soc. Sect. B* **66**, 377 (1953).
- [49] J. A. Wilson and A. D. Yoffe, The transition metal dichalcogenides discussion and interpretation of the observed optical, electrical and structural properties, *Adv. Phys.* **18**, 193 (1969).
- [50] A. Stesmans, S. Iacovo, and V. V. Afanas'Ev, ESR study of P-type natural 2H-polytype MoS<sub>2</sub> crystals: The As acceptor activity, *Appl. Phys. Lett.* **109**, 172104 (2016).
- [51] A. Pisoni, J. Jacimovic, O. S. Barišić, A. Walter, B. Náfrádi, P. Bugnon, A. Magrez, H. Berger, Z. Revay, and L. Forrő, The role of transport agents in MoS<sub>2</sub> single crystals, *J. Phys. Chem. C* **119**, 3918 (2015).
- [52] B. Schoenaers, A. Stesmans, and V. V. Afanas'Ev, ESR identification of the nitrogen acceptor in 2H-polytype synthetic MoS<sub>2</sub>: Dopant level and activation, *AIP Adv.* **7**, 105006 (2017).
- [53] M. Cook, R. Palandech, K. Doore, Z. Ye, G. Ye, R. He, and A. J. Stollenwerk, Influence of interface coupling on the electronic properties of the Au/MoS<sub>2</sub> junction, *Phys. Rev. B* **92**, 201302 (2015).
- [54] J. R. Lince, D. J. Carré, and P. D. Fleischauer, Schottky-barrier formation on a covalent semiconductor without Fermi-level pinning: The metal-MoS<sub>2</sub>(0001) interface, *Phys. Rev. B* **36**, 1647 (1987).
- [55] W. Nolting, C. Durcan, A. J. Narasimham, and V. P. LaBella, Nanoscale Schottky barrier mapping of thermally evaporated and sputter deposited W/Si(001) diodes using ballistic electron emission microscopy, *J. Vac. Sci. Technol., B* **34**, 04J110 (2016).
- [56] W. Nolting, C. Durcan, and V. P. LaBella, Detection of silicide formation in nanoscale visualization of interface electrostatics, *Appl. Phys. Lett.* **110**, 141606 (2017).
- [57] W. Nolting, C. Durcan, S. Gassner, J. Goldberg, R. Balsano, and V. P. Labella, Nanoscale schottky barrier visualization utilizing computational modeling and ballistic electron emission microscopy, *J. Appl. Phys.* **123**, 245302 (2018).
- [58] B. H. Moon, G. H. Han, H. Kim, H. Choi, J. J. Bae, J. Kim, Y. Jin, H. Y. Jeong, M. K. Joo, Y. H. Lee, and S. C. Lim, Junction-structure-dependent Schottky barrier inhomogeneity and device ideality of monolayer MoS<sub>2</sub> Field-effect transistors, *ACS Appl. Mater. Interfaces* **9**, 11240 (2017).